Multiwavelength photometry in the Globular Cluster M2[1]

E. Dalessandro[2,3,4], G. Beccari[5], B. Lanzoni[2], F.R. Ferraro[2], R. Schiavon[6], R.T. Rood[7]

[2] *Dipartimento di Astronomia, Università degli Studi di Bologna, via Ranzani 1, I–40127 Bologna, Italy*

[3] *ASI,Centro di Geodesia Spaziale, contrada Terlecchia, I-75100, Matera, Italy*

[4] *INAF, Osservatorio Astronomico di Bologna, via Ranzani 1, I–40127 Bologna, Italy*

[5] *European Space Agency, Space Science Department, Keplerlaan 1, 2200 AG Noordwijk, Netherlands*

[6] *Gemini Observatory, 670 North A'ohoku Place, Hilo, HI 96720, USA*

[7] *Astronomy Department, University of Virginia, P.O. Box 400325, Charlottesville, VA, 22904*

ABSTRACT

We present a multiwavelength photometric analysis of the globular cluster M2. The data-set has been obtained by combining high-resolution (HST/WFPC2 and ACS) and wide-field (GALEX) space observations and ground based (MEGACAM-CFHT, EMMI-NTT) images. The photometric sample covers the entire cluster extension from the very central regions up to the tidal radius and beyond. It allows an accurate determination of the cluster center of gravity and other structural parameters derived from the star count density profile. Moreover we study the BSS population and its radial distribution. A total of 123 BSS has been selected, and their radial distribution has been found to be bimodal (highly peaked in the center, decreasing at intermediate radii and rising outward), as already found in a number of other clusters. The radial position of the minimum of the BSS distribution is consistent with the radius of avoidance caused by the dynamical friction of massive ($1.2 M_\odot$) objects over the cluster age. We also searched for gradients in the red giant branch (RGB) and the asymptotic giant branch (AGB) populations. At the 2σ level we found an overabundance of AGB stars within the core radius and confirmed the result of Sohn et al.(1996) that the central region of M2 is bluer than the outer part. We show that the latter is due to a deficit of very luminous RGB stars in the central region.

Subject headings: Globular clusters: individual (M2); stars: evolution - binaries: general - blue stragglers

1.   INTRODUCTION

In this paper we present multiwavelength observations of the Galactic globular cluster M2 (NGC 7089). These observations are part of a large project aimed at characterizing the ultraviolet (UV) bright populations of old stellar systems and determining the impact of stellar dynamics on the cluster evolution by studying their "exotic" populations. As in our previous study of NGC 1904 (Lanzoni et al. 2007b), we use HST high-resolution UV and optical data for the high density central region of the cluster and a combination of ground-based wide-field optical data (MEGACAM-CFHT and EMMI-NTT) and UV data from the Galaxy Evolution Explorer (GALEX) for the cluster outskirts. Combining these samples allows an accurate determination of the center of gravity, the stellar density profile and the structural parameters. In this paper we focus on the Blue Straggler Star (BSS) population as tracers of the dynamical state of the host cluster and products of the interplay between stellar evolution and stellar dynamics. We also discuss possible radial gradients in the Asymptotic Giant Branch (AGB) stars and other stellar populations. We defer a discussion of the Horizontal Branch (HB) population to a future paper.

In the optical color-magnitude diagram (CMD) BSSs are bluer (hotter) and brighter than the main-sequence (MS) stars, thus mimicking a stellar population significantly younger than the "normal" cluster stars. As shown by Shara et al. (1997), BSSs are more massive than normal stars, suggesting that some mass-increasing mechanism drives their formation. Possible explanations involve mass transfer between binary companions, the merger of a binary system, and the collision between single and/or binary stars (McCrea 1964; Zinn & Searle 1976). Clear differentiation among these possibilities is difficult, since primordial binaries can sink to the cluster center, where stellar collisions may significantly alter their evolution. Similarly, gravitational interactions can generate new binary systems and possibly kick them out of the cluster core. With this caveat, we define primordial binary BSS

---

[1]Based on observations with the NASA/ESA *HST* (Prop. 8709 and Prop.10775), obtained at the Space Telescope Science Institute, which is operated by AURA, Inc., under NASA contract NAS5-26555. Also based on EMMI observations (Prop 079.D-0325) collected at the European Southern Observatory, La Silla, Chile. Based on observations with MegaPrime/MegaCam, a joint project of CFHT and CEA/DAPNIA, at the Canada-France-Hawaii Telescope (CFHT), which is operated by the National Research Council (NRC) of Canada, the Institute National des Sciences de l'Univers of the Centre National de la Recherche Scientifique of France, and the University of Hawaii. It is also based on GALEX observations (program GI-056)

(PB-BSS) those formed by mass transfer processes (possibly up to complete coalescence) in primordial binaries which evolved in isolation in the cluster. Collisional BSS (COL-BSS) are those generated by mechanisms where stellar collisions played a major role. We therefore expect PB-BSS to mainly populate the external regions of the cluster, where the collision probabilities are lower. COL-BSSs preferentially form in the central regions because of the higher stellar densities [2]. These formation mechanisms may work simultaneously with different efficiency depending on the environment (Fusi Pecci et al. 1993; Ferraro et al. 1999, 2003; Bellazzini et al 2002).

Observed BSS radial distributions have been particularly important in demonstrating the complex interplay of the various phenomena. Typically the BSS radial distributions have been found to be bimodal (peaked in the clusters center and outskirts and with a dip at intermediate radii; see references in Dalessandro et al. 2008a; see also Beccari et al. 2008 for M53). Only two clusters deviate from this pattern: ω Centauri (ω Cen, Ferraro et al. 2006b) and NGC 2419 (Dalessandro et al. 2008b). In those clusters the BSS radial distribution is indistinguishable from that of the other cluster stars. Simple dynamical simulations (Mapelli et al. 2004, 2006; Lanzoni et al. 2007a) suggest that the observed bimodality can be modelled assuming that PB-BSSs and COL-BSSs co-exist in the same cluster with relative fractions that vary from one case to another. The radial distributions observed in NGC 2419 and ω Cen could be the observational evidence that mass-segregation processes have played a minor role in altering the BSS radial distributions and that the observed BSS population is mainly composed of PB-BSSs.

2. OBSERVATIONS AND DATA REDUCTION

2.1. The data sets

The present work is based on a combination of different high-resolution and wide-field data-sets. The high resolution set consists of a series of WFPC2 and ACS images taken at various wavelengths ranging from the UV to the optical bands. The WFPC2 images (Prop 8709, P.I. Ferraro) were obtained through the UV filters $F160BW$ and $F255W$ with total exposure times $t_{\exp} = 1800\,\mathrm{s}$ and $t_{\exp} = 2000\,\mathrm{s}$ respectively, and through the optical filters

---

[2]A distinction between PB-BSS and COL-BSS requires high resolution spectroscopic studies (see the case of 47 Tucane in Ferraro et al. 2006): in fact characteristic chemical signatures are expected on the surface of PB-BSSs so that accurate measurement of the stellar surface abundances can distinguish between the two types of stars (Sarna & de Greve 1996), while they are not predicted in the case of COL-BSSs (Lombardi et al. 1995).

$F336W$ and $F555W$ with exposure times $t_{\rm exp} = 1800\,{\rm s}$ and $t_{\rm exp} = 106\,{\rm s}$. The center of the cluster is located in the WF2 chip (pixel scale $\sim 0.1''{\rm pixel}^{-1}$). The photometric reduction of these data was performed using ROMAFOT (Buonanno et al. 1983) a package developed to obtain accurate photometry in crowded regions and specifically optimized to handle under-sampled point spread functions (Buonanno & Iannicola 1989). The ACS data-set is a series of images in $F606W$ ($\sim V$) and $F814W$ ($\sim I$) with $t_{\rm exp} = 20\,{\rm s}$ and $t_{\rm exp} = 20\,{\rm s}$ (Prop. 10775, P.I. Sarajedini). The images were corrected for geometrical distortions and effective flux (Sirianni et al. 2005). The photometric reduction was performed using the photometric package SExtractor (Bertin & Arnouts 1996). The wide field set is composed of data obtained with 3 different instruments:

a) EMMI-ESO-NTT – B and V images (with $t_{\rm exp} = 40\,{\rm s}$ and $t_{\rm exp} = 20\,{\rm s}$) were taken with the ESO Multi Mode Instrument (EMMI) at the NTT during an observing run in July 2007 (P.I. Ferraro, Prop 079.D-0325). We used the EMMI Red CCD that is composed of 2 chips of 2048×4093 pixels each with a pixel scale of about $0.33''{\rm pixel}^{-1}$ and an effective field of view (FOV) of about $9.0' \times 9.9'$. The images were corrected for bias and flat field by using standard IRAF tools. The data reduction was performed with SExtractor (Bertin & Arnouts 1996).

b) MEGACAM-CFHT – A combination of short and long MEGACAM exposures taken through the g ($t_{\rm exp} = 24\,{\rm s}$ and $t_{\rm exp} = 240\,{\rm s}$) and r ($t_{\rm exp} = 48\,{\rm s}$ and $t_{\rm exp} = 480\,{\rm s}$) filters was retrieved from the Canadian Astronomy Data Centre (CADC4). The wide field imager MEGACAM is mounted at Canadian-French-Hawaiian Telescope (CFHT) and consists of 36 CCDs of 2048×4612 pixels each. For this work we used two different pointings in which the cluster center is located between chip #27 and chip #36, and #19 and #28 respectively. This allowed a coverage of an area of $2 \times 1\,{\rm deg}^2$ and a complete sampling of the cluster well beyond its tidal radius. The data were pre-processed, astrometrized and calibrated by using the Elixir pipeline. We performed the data reduction using SExtractor (Bertin & Arnouts 1996). Each chip in each image was reduced separately and then combined with all the others for obtaining a catalog with g and r magnitudes and positions of the detected stars.

c) GALEX – A complete coverage of the cluster in the UV bands was obtained using GALEX data (FOV of about $1\,{\rm deg}^2$) through the FUV (1350–1750Å) and NUV (1750–2800Å) detectors (program GI-056, P.I. Schiavon). Because of the high concentration of M2 and the low angular resolution of the GALEX channels ($4''$ in FUV and $6''$ in NUV) we used the GALEX data only for $r \geq 200''$ from the center of gravity (see below). The reduction of GALEX data was performed independently for each filter with DAOPHOTII/ALLFRAME (Stetson 1987).

3. Definition of the photometric catalogs

3.1. Astrometry and photometric calibration

All the catalogs were put on the absolute astrometric system using a large number of stars in common with the Sloan Digital Sky Survey (SDSS) catalog. As a first step we obtained the astrometric solution of the 72 chips of MEGACAM by using the procedure described in Ferraro et al. (2001, 2003) and a specific cross-correlation tool. All the stars in common with the GALEX, EMMI and HST samples were then used as secondary astrometric standards in order to put all the catalogs in the same astrometric system. Several hundred astrometric standards have been found in each step, allowing a very precise astrometry for each catalog. At the end of the procedure the estimated error in the absolute positions, both in right ascension (α) and declination (δ) is about $0.2''$.

All the WFPC2 magnitudes (m_{160}, m_{255}, m_{336} and m_{555}) were calibrated in the STMAG system using the equations and zeropoints listed in Holtzmann et al. (1995) and the same procedure described in Ferraro et al. (1997, 2001). Then the stars in common between the other catalogs and the WFPC2 sample were used to transform all the magnitudes to the same photometric system. In particular, the $F606W$ of the ACS catalog, the EMMI instrumental V magnitudes and MEGACAM g magnitudes were transformed to the V STMAG by using appropriate color equations. The EMMI B instrumental magnitudes were put in the STMAG system. The ACS $F814W$ magnitudes were calibrated in the STMAG system using the prescriptions of Sirianni et al. (2005), and the r MEGACAM mag was transformed to the SDSS system. The GALEX instrumental FUV and NUV magnitudes were calibrated to STMAG system using the stars in common with the WFPC2.

3.2. Center of Gravity

The center of gravity has been obtained following the procedure adopted in our previous work (see for example Lanzoni et al. 2007b). A first estimate of the cluster center was performed by eye on the WF2 chip of the WFPC2 image, then the exact measure of C_{grav} was obtained by means of an iterative procedure that averages the absolute positions of stars lying within $\sim 10''$ from the first guess center. In order to avoid biases and spurious effects, we considered two samples with two different limiting magnitudes ($V < 19.7$ and $V < 19.2$). The values of C_{grav} obtained with the two samples agree within $1''$. We adopt the mean value as the best estimate of C_{grav}: $\alpha = 21^{\text{h}}33^{\text{m}}27^{\text{s}}$ ($RA = 323.3623340$) and $\delta = -0°49'22.8''$ ($Dec = -0.82304665$) . This new determination is substantially different from the center reported by Harris et al. (1996) on the basis of the surface brightness profile

and using photographic plates: our C_{grav} is located at $\sim 35''$ west ($\Delta\alpha \sim 35''$, $\Delta\delta \sim 0''$) from Harris center.

3.3. Sample definition

Once all the data-sets have been photometrically homogenized and put in the same reference frame, and the cluster center has been determined, we have built a single catalog by combining the following sub-samples: *i)* the WFPC2 sample, composed of all the stars detected in the WFPC2 FOV; *ii)* the ACS sample, comprising all the stars in the ACS FOV complementary to the WFPC2 one; *iii)* the EMMI sample, complementary to the previous two and including only stars with distance $r < 200''$ from C_{grav} and *iv)* the MEGA-CAM/GALEX sample made of stars with $r \geq 200''$ included in the MEGACAM FOV (of course only a fraction of these stars also has GALEX magnitudes). The criteria used for these definitions have been chosen to sample the highly crowded central regions of the cluster with the highest spatial resolution and UV band data (thus to maximally limit the effects of photometric errors and stellar blends), while covering the entire cluster extension by means of wide-field images. The maps of the adopted samples are shown in Figures 1 and 2. In Fig. 3 the (V, $U - V$) CMD of the WFPC2 sample is shown.

3.4. Density profile

We have determined the projected density profile of M2 by measuring the star counts over the entire cluster extension. Only stars with $15.2 < V < 19.2$ in the combined sample, covering the cluster extension from C_{grav} to $r = 1800''$ were considered (see Figs. 4 and 5). The area was divided in 36 annuli all centered on C_{grav}. Each annulus was divided into an adequate number of sub-sectors in which the stellar density has been calculated as the ratio between the number of stars and the sub-sector area. For each annulus the resulting density is given by the average of the corresponding sub-sector densities and the error is quoted as the square root of the variance of the sub-sector densities. In this procedure we have also taken into account the incomplete area coverage of the most external annuli and the largest CCD gap in the MEGACAM FOV.

The observed density profile is plotted in Fig. 6. The sample nicely covers the entire cluster extension. The four outermost annuli (with $r > 600''$) show a flattening of star counts giving a direct estimate of the stellar background in the cluster direction: for $15.2 < V < 19.2$ the background star density is ~ 0.7 stars/arcmin^2. The observed profile is well reproduced

by an isotropic single-mass King model with concentration $c \simeq 1.51$ and core radius $r_c \simeq 17''$. The corresponding tidal radius is $r_t \simeq 550''$. Since there is an uncertainty of about 15% in the determination of r_t, in our analysis below we will consider all stars lying within $r < 650''$. The newly determined cluster parameters are substantially different from those reported by Harris et al. (1996) based on the luminosity center and the surface brightness distribution ($c = 1.8$ and $r_c = 20''$) and from the even higher concentration model found by Pryor & Meylan (1993; $c = 1.9$ and $r_c = 20''$). As shown in Fig. 6 (dashed line), a King model with the parameters quoted by Harris et al. (1996) does not reproduce the observed profile. On the contrary, a reasonable agreement (within the errors) is found with the values estimated by McLaughlin & van der Marel (2005; $c = 1.59$ and $r_c = 19''$). Assuming a distance modulus $(m - M)_V = 15.49$ and a reddening $E(B - V) = 0.06$ (Harris et al. 1996) we find a real distance $d \simeq 12.5\,\mathrm{kpc}$, and a core radius $r_c \simeq 1.02\,\mathrm{pc}$.

The best-fit model reproduces the observed profile out to $400''$ very well, while at larger distances the observed star counts show an excess with respect to the model. While this discrepancy is not statistically significant, it deserves further investigation since it could be the signature of tidal distortion in the outer regions (see Leon et al. 2000 for more details). Another interesting feature of density profile is that the innermost point seems to deviate from the canonical flat-core King model. This is also worthy of future investigation since similar features might be related to the presence of an intermediate mass-black hole (e.g. Miocchi 2007, Lanzoni et al. 2007c).

4. THE BSS AND REFERENCE POPULATION SELECTION

4.1. The BSS selection

In this section we describe the procedure that we have followed to select the BSS population and to construct the BSS radial distribution in M2. At the UV wavelengths, hot populations like BSSs and extreme-HB stars are the brightest objects, while cool populations (like red giant branch – RGB – stars) appear quite faint (see Figs. 7 and 10). Because of this, we always prefer to use the UV-CMD as the reference plane for the BSS selection. Moreover, since the HST spatial resolution dramatically reduces problems connected with crowding and blends, we have primarily selected the BSS population by considering the WFPC2 sample in the $(m_{255}, m_{255} - U)$ plane. In order to avoid contamination from the sub-giant branch (SGB) stars, we selected only stars with $m_{255} < 19.55$, that is about 1 magnitude brighter than the turn-off (TO) point ($m_{255} \simeq 20.5$). The number of BSS thus selected in the WFPC2 sample is 82.

As in previous studies, we used the UV-selected BSS in common with the ACS sample to define a selection box in the $(V, V − I)$ plane. We have adopted a limiting magnitude $V \sim 19.2$, and the red edge is at $(V − I) = 0.55$ (see Fig. 8). The total number of BSS found in the ACS sample is 20. In the EMMI catalog the BSS have been selected in the $(V, B−V)$ CMD, using the same cut in the V filter as for ACS sample. Considering the quality of the diagram the color limit was set to $(B − V) < 0.32$ to avoid spurious detections and blends from TO and SGB stars: 9 BSS have been selected in this way (see Fig. 9). In the most external region sampled by our observations $(r \geq 200'')$ the combination of the MEGACAM and the GALEX samples allows the construction of an UV CMD. Since both the GALEX NUV and the HST m_{255} magnitudes have been calibrated on the STMAG photometric system (see Sect. 3.1), we have used the same threshold $(NUV < 19.55)$ adopted for the WFPC2 sample to define the selection box in the $(NUV, NUV − V)$ plane. The result is shown in Fig. 10, where 12 BSS have been selected for $r \geq 200''$. The right panel of Fig. 10 shows the location of the selected BSS in the $(V, V − r)$ plane. In summary a total of 123 BSS have been selected in M2 (see Table 1).

4.2. The reference populations

As discussed in other papers (see Ferraro 2006a and references in Dalessandro et al. 2008a) we also need to select a reference population which is representative of the "normal" cluster population. As in other works of this series, we have used the HB and RGB stars as reference populations. The selection of the RGB stars has been performed in the optical planes. For all of the samples a magnitude cut at $V < 18$ has been adopted. However for our analysis only stars with $V > 16$ were used in order to avoid saturated stars in the ACS and MEGACAM/GALEX sample (Fig. 8 and Fig. 10). The color limits of the selection boxes have been chosen to follow the RGB ridge mean line in each CMD while avoiding regions with high probability of field star contamination (the selected RGB stars are marked with empty squares in Fig. 8, 9 and 10). We found 2121 RGB within $r < 650''$ (1223 in WFPC2, 460 in ACS, 270 in EMMI and 168 in MEGACAM/GALEX samples, respectively). The magnitude range of the RGB reference population is the same as that adopted for the "faint" RGB discussed below.

In the WFPC2 and MEGACAM/GALEX samples the HB stars have been selected on the basis of their positions in the $(m_{255}, m_{255} − V)$ and (NUV,NUV-V) CMDs respectively (see left panel of Fig. 10 for the wide-field sample). The positions in the optical MEGA-CAM/GALEX plane of the selected HB stars (Fig. 10 right panel) have been used to define the selection box for the ACS and EMMI samples (see Figs. 8 and 9). By cross-correlating

our catalog with the catalogs of RR Lyrae stars found by Lee & Carney (1999) and Lazaro et al. (2006), we have identified all of the 42 known variables (they are marked as asterisks in Fig. 7, 8, 9 and 10) and we have included them in our HB sample. The total number of HB stars within $r < 650''$ is 875 (525 in WFPC2, 184 in ACS, 104 in EMMI and 62 in MEGACAM/GALEX samples).

5. Results

5.1. The BSS radial distribution

Having defined the reference populations we can now examine the BSS radial distribution. The BSS cumulative radial distribution is shown in Fig. 11 with the distributions of the HB and RGB stars shown for comparison. The BSS population is more segregated in the central regions and less concentrated in the outer parts than either the HB and the RGB stars. The KS test gives a probability of $\sim 10^{-6}$ (4σ significance level) that the radial distribution of the BSS is extracted from the same parent distribution of the reference population.

For a more quantitative analysis we computed the population ratios $N_{\rm BSS}/N_{\rm HB}$ and $N_{\rm BSS}/N_{\rm RGB}$ (where $N_{\rm pop}$ is the number of stars belonging to a given population) in 6 concentric annuli centered on $C_{\rm grav}$. To do this we had to evaluate the impact of field star contamination on each population. The field stars predominantly lie in a vertical sequence at $0.2 < (V - r) < 0.5$ and dramatically affect the RGB population (see Fig 5 right panel). An estimate of the field star contamination can be directly obtained from our sample by considering an annulus at $1900'' < r < 2400''$ ($\sim 70\%$ of which is sampled by the MEGACAM data) far beyond the tidal radius of the cluster ($r_t \sim 550''$). We counted the number of field stars in this annulus lying within the BSS, HB and RGB selection boxes shown in Figs. 8, 9, and 10, and we derived the following values for their density: $\rho_{\rm BSS} \sim 0.01$ stars/arcmin^2, $\rho_{\rm RGB} \sim 0.06$ stars/arcmin^2, while no field stars have been found within the HB selection box. These values have been used to statistically decontaminate the star counts in each annulus.

The star counts for each annulus are listed in Table 2. These values have been used to compute the ratios $N_{\rm BSS}/N_{\rm HB}$ and $N_{\rm BSS}/N_{\rm RGB}$. The radial distribution of these ratios is shown in Fig. 12 (central and upper panels, respectively). They are clearly bimodal, with a high BSS frequency in the central and outer regions, and with a broad minimum at about $120''$ ($\sim 9r_c$) from $C_{\rm grav}$. On the contrary the $N_{\rm HB}/N_{\rm RGB}$ ratio (plotted in the bottom panel of Fig. 12) shows a flat distribution across the cluster extension, as expected for "normal" populations. As a further confirmation of the BSS bimodality, we also computed the double

normalized ratio as defined in Ferraro et al. (1993):

$$R_{\text{pop}} = \frac{N_{\text{pop}}/N_{\text{pop}}^{\text{tot}}}{L^{\text{samp}}/L_{\text{tot}}^{\text{samp}}}.$$

where pop = BSS, HB. The total sampled luminosity ($L_{\text{tot}}^{\text{samp}}$), as well as the luminosity sampled in each annulus (L^{samp}), has been estimated from the King model by using the cluster structural parameters, distance modulus and reddening quoted in Section 3.3, and the central surface brightness reported by Harris et al. (1996). The incomplete spatial coverage due to the largest ($\sim 1'$) gap between the MEGACAM CCDs has been taken into account. As shown in Fig. 13, R_{HB} is constant with a value close to 1 out to $r = 650''$. This is just as expected: the fraction of HB (as any post-MS) stars is proportional to the fraction of sampled light, as shown in Renzini & Fusi Pecci (1988). Conversely the radial distribution of the BSS double normalized ratio (R_{BSS}) confirms the bimodal behaviour: it is peaked in the central regions, decreases to a minimum value at about $9r_c$ and then rises again in the cluster outskirts.

The location of this minimum at $r \sim 9r_c$ can be related to the dynamical evolution of the cluster and in particular to the radius of avoidance (r_{avoid}). This parameter is defined as the radius within which all the stars as massive as $1.2M_\odot$ (the assumed mass for BSSs) have already sunk to the center because of mass segregation (Mapelli et al. 2004, 2006). Using the dynamical friction time-scale formula (e.g. Mapelli et al. 2006) under the assumption of a cluster age $t = 12\,\text{Gyr}$, a central velocity dispersion of $\sigma_0 = 8.2\,\text{km s}^{-1}$ (Pryor & Meylan 1993), we obtained $r_{\text{avoid}} \sim 7r_c$. This position is fully compatible with the position of the observed minimum.

5.2. The AGB problem

Beccari et al. (2006a) found a significant overabundance of AGB stars in the very central regions of 47 Tuc. This excess could be due to contamination of genuine AGBs by massive (1.1–$1.5\,M_\odot$) objects in late evolutionary stages (e.g. in the horizontal branch phase, as suggested by Sills et al. 2008). Presumably these objects arise from binary systems (mainly BSSs) segregated in the cluster core because of dynamical effects. To search for a similar result in M2, we used the WFPC2 and the EMMI sample where the brightest evolutionary sequences are well defined up to the RGB tip at $V \sim 13$. We selected AGB stars in the (V, $U - V$) plane for the WFPC2 sample and in the (V, $B - V$) for the EMMI sample as shown in Fig. 14. It was not possible to use either the ACS or the MEGACAM/GALEX samples because of saturation problems.

To study the radial distribution we divided the covered region into 5 concentric annuli centered on C_{grav} and counted the number of AGBs and HBs lying in each annulus. It was not possible to do a statistical decontamination of the AGB population because the MEGACAM/GALEX sample saturates at $V \sim 15.5$. However, we would expect that in the central regions it does not appreciably affect the observed radial distribution. Fig. 15 upper panel shows the behaviour of the population ratios $N_{\mathrm{AGB}}/N_{\mathrm{HB}}$ as a function of the distance from the cluster center. As apparent from the figure, while the mean value of the 4 outermost annuli is $\sim 0.12 \pm 0.03$, fully consistent with the value expected from the evolutionary timescales (Renzini & Fusi Pecci 1988), the ratio turns out to be higher ($\sim 0.19 \pm 0.03$) in the outermost annulus (corresponding to r_c). This central overconcentration of the AGB population corresponds to an excess of about 30% (or 9-10 more stars) in the first annulus. This value is compatible with the life-times and populations ratios computed by Sills et al. (2008) for evolved collisional products, supporting the idea of a possible contamination by evolved BSS. To further investigate this feature we also computed the double normalized ratio. The incomplete spatial coverage has been taken into account. The radial distribution of R_{AGB} (see Fig. 15 bottom panel) fully confirms this behaviour, showing a central peak ($R_{\mathrm{AGB}} \sim 1.4$) within r_c, while in the outer part the ratio remains constant at $R_{\mathrm{AGB}} \sim 1$ fully in agreement with R_{HB}.

Purely on the basis of small number statistics introduced by binning, the AGB central peak is marginally significant ($< 2\sigma$). However the significance of the peak can also be evaluated with a KS test on the cumulative distribution, which is shown in Fig. 16. The probability that the AGBs are drawn from a different distribution from the HBs is 93% ($\sim 1.8\sigma$). The BSS distribution is also shown in Fig. 16. While AGBs are more concentrated than HBs, they are less concentrated than BSSs, with a 98% probability that they are extracted from a different parent family. In this respect they are different from the AGBs in 47 Tuc where AGBs and BSSs have similar radial distributions.

5.3. Color gradients

Sohn et al. (1996), hereafter S96, found that M2 has a radial color gradient, in the sense that the central regions are bluer than the outer parts, with a variation of about $(B - V) \sim 0.1$. To investigate this interesting feature we computed the $(U - V)$ integrated color within $90''$ from C_{grav} which approximately corresponds to the region used by S96. We divided the WFPC2 sample in 5 concentric annuli (the first corresponding to r_c), and computed the color of each annulus from the resolved stars by considering three different magnitude cuts: $V < 16$, $16 \leq V < 20$ and $V < 20$. As shown in Fig. 17 (upper panel)

we found that when only the brightest stars are included ($V < 16$, black and open dots in Fig. 17) a color difference $\Delta(U - V) \sim 0.18$ between the center (bluer) and the outer annuli is apparent. Even if this is a less than 2σ result, it is consistent with the finding of S96. When also fainter stars are included (i.e. for $V < 20$), the color gradient decreases, and if the brightest stars are excluded ($16 \leq V < 20$) it completely disappears and $(U - V)$ remains constant all over the considered radial range. To further investigate this behaviour we made the same computation for the ACS sample using the $(V - I)$ color. In this sample saturation occurs at about $V = 15$, so the test is limited to the population with $16 < V < 20$. No color gradient is visible in the bottom panel of Fig. 17. Our results therefore indicate that the observed color gradient is due to the brightest stars and not to an over-concentration of BSSs or blue faint objects. This seems in disagreement with the conclusion of S96, who found the color gradient only when using resolved stars with $V < 16$. However, as already discussed by these authors, the poor seeing conditions and the spatial resolution of the instrument ($0.56''\,\text{pixel}^{-1}$) used in their analysis did not allow them to sample all the populations with acceptable photometric accuracy. To more deeply understand the origin of the detected color gradient, we further investigated the properties of the brightest populations in the very central regions of M2. Since the AGB is 0.2-0.3 mag bluer than the RGB in $(U - V)$, we first investigated whether the AGB central excess (Sect.5.2) could account for the observed color gradient. We therefore artificially cancelled the AGB central peak, by randomly excluding 10 stars from the innermost bin, and re-computed the central color: this still yields a center bluer than the exterior. Very bright RGB stars therefore remain the only candidates. In order to test this hypothesis we compared the radial distribution of the brightest portion of the RGB ($V < 16$) in the WFPC2 sample (see Fig. 14, left panel) to the faint ($V \geq 16$) one. The radial distributions of these populations clearly show that the brightest giants are less concentrated than the faintest ones, with a 99% probability (about 2.5σ) that they are extracted from a different parent family (see Fig. 16 and the upper panel of Fig. 18). We have therefore re-computed the central color after having artificially increased the number of bright RGBs in the innermost bin, thus to flatten the radial distribution of the bright-to-faint RGB ratio (to this purpose, we have randomly extracted 25 bright RGBs from the observed luminosity function). This completely removes the color gradient (bottom panel of Fig. 18). Hence we conclude the the color gradient found by S96 and confirmed here is due to a deficit of bright RGB stars in the center rather than a surplus of fainter blue stars.

6. Summary

The BSS population of M2 can be characterized as what is emerging as *"normal"*: a bimodal radial distribution with a minimum in the zone of avoidance, and with a value of

the central BSS specific frequency ($N_{\mathrm{BSS}}/N_{\mathrm{HB}}$) which is also typical. Bimodal distributions are a very common feature of the Galactic GC BSS populations (Dalessandro et al. 2008a). Only two clusters, NGC 2419 and ω Cen, deviate significantly from this pattern. Both of these systems are very large. There is even some doubt that ω Cen is a true GC (Bekki & Freeman 2003). Of the bimodal clusters only two, NGC 6388 (Dalessandro et al. 2008a) and NGC 5024 (Beccari et al. 2008), have minima in their BSS radial distributions which differ significantly from r_{avoid}. Presumably this arises because of a lower efficiency of the dynamical friction in these two clusters, for reasons yet to be explained.

As Beccari et al. (2006) found for 47 Tuc, we find an excess of AGB stars in the center of M2. Because of the smallish sample size, the excess is only marginally significant, and unlike in 47 Tuc, the AGB population is not as concentrated as the BSS one.

In agreement with S96 we find that the integrated color of the central region of M2 is bluer that the exterior. We show that this color gradient is due to a deficit of bright RGB stars, and not to an excess of faint blue objects, such as BSS or HB stars. A similar deficit of bright RGB stars has also been found in the very massive GC NGC 2808 (Sandquist et al. 2007). They do not explore the radial dependence of their result, and neither of the two mechanisms they discuss for producing a deficit (neutrino losses and extra mass loss) would have an obvious radial dependence. We view our AGB surplus and bright RGB deficit as suggestive—given the short lifetime in these phases it is impossible to do better than 2σ in M2 or any single cluster. If similar results are found in other clusters, there would be interesting consequences for stellar evolution theory and stellar population studies. Given this, it would be highly desirable that future photometric studies of GCs were designed in such a way that unsaturated photometry of the brightest stars was possible.

REFERENCES

Beccari, G., Ferraro, F. R., Possenti, A., Valenti, E., Origlia, L., & Rood, R. T. 2006a, AJ, 131, 2551

Beccari, G., et al. 2008, ApJ, 679, 712

Bellazzini, M., Fusi Pecci, F., Messineo, M., Monaco, L., & Rood, R. T. 2002, AJ, 123, 1509

Bertin, E., & Arnouts, S. 1996, A&AS, 117, 393

Bekki, K., & Freeman, K. C. 2003, MNRAS, 346, L11

Buonanno, R., Buscema, G., Corsi, C. E., Ferraro, I., & Iannicola, G. 1983, A&A, 126, 278

Buonanno, R., & Iannicola, G. 1989, PASP, 101, 294

Dalessandro, E., Lanzoni, B., Ferraro, F. R., Rood, R. T., Milone, A., Piotto, G., & Valenti, E. 2008a, ApJ, 677, 1069

Dalessandro, E., Lanzoni, B., Ferraro, F. R., Vespe, F., Bellazzini, M., & Rood, R. T. 2008b, ApJ, 681, 311

Ferraro, F. R., Fusi Pecci, F., Cacciari, C., Corsi, C., Buonanno, R., Fahlman, G. G., & Richer, H. B. 1993, AJ, 106, 2324

Ferraro, F. R., Paltrinieri, B., Fusi Pecci, F., Cacciari, C., Dorman, B., Rood, R. T., Buonanno, R., Corsi, C. E., Burgarella, D., & Laget, M., 1997, A&A, 324, 915

Ferraro, F. R., Paltrinieri, B., Rood, R. T., & Dorman, B. 1999a, ApJ 522, 983

Ferraro, F. R., D'Amico, N., Possenti, A., Mignani, R. P., & Paltrinieri, B. 2001, ApJ, 561, 337

Ferraro, F. R., Sills, A., Rood, R. T., Paltrinieri, B., & Buonanno, R. 2003, ApJ, 588, 464

Ferraro, F. R., et al. 2006a, ApJ, 647, L53

Ferraro, F. R., Sollima, A., Rood, R. T., Origlia, L., Pancino, E., & Bellazzini, M. 2006b, ApJ, 638, 433

Fusi Pecci, F., Ferraro, F. R., Bellazzini, M., Djorgovski, S., Piotto, G., & Buonanno, R. 1993, AJ, 105, 1145

Harris, W.E. 1996, AJ, 112, 1487

Holtzman, J. A., Burrows, C. J., Casertano, S., Hester, J. J., Trauger, J. T., Watson, A. M., & Worthey, G. 1995, PASP, 107, 1065

Lanzoni, B., Dalessandro, E., Ferraro, F. R., Mancini, C., Beccari, G., Rood, R. T., Mapelli, M., & Sigurdsson, S. 2007a, ApJ, 663, 267

Lanzoni, B., et al. 2007b, ApJ, 663, 1040

Lanzoni, B., Dalessandro, E., Ferraro, F. R., Miocchi, P., Valenti, E., & Rood, R.T. 2007c, ApJ, 668, L139

Lázaro, C., Ferro, A. A., Arévalo, M. J., Bramich, D. M., Giridhar, S., & Poretti, E. 2006, MNRAS, 372, 69

Lee, J.-W., & Carney, B. W. 1999, AJ, 117, 2868

Leon, S., Meylan, G., & Combes, F. 2000, A&A, 359, 907

Lombardi, J. C. Jr., Rasio, F. A., & Shapiro, S. L. 1995, ApJ, 445, L117

Mapelli, M., Sigurdsson, S., Colpi, M., Ferraro, F. R., Possenti, A., Rood, R. T., Sills, A., & Beccari, G. 2004, ApJ, 605, L29

Mapelli, M., Sigurdsson, S., Ferraro, F. R., Colpi, M., Possenti, A., & Lanzoni, B. 2006, MNRAS, 373, 361

McLaughlin, D. E., & van der Marel, R. P. 2005, ApJS, 161, 304

McCrea, W. H. 1964, MNRAS, 128, 147

Miocchi, P. 2007, MNRAS, 381, 103

Pryor C., & Meylan G., 1993, Structure and Dynamics of Globular Clusters. Proceedings of a Workshop held in Berkeley, California, July 15-17, 1992, to Honor the 65th Birthday of Ivan King. Editors, S.G. Djorgovski and G. Meylan; Publisher, Astronomical Society of the Pacific, Vol. 50, 357

Renzini, A., & Fusi Pecci, F. 1988, ARA&A, 26, 199

Sandquist, E. L., & Martel, A. R. 2007, ApJ, 654, L65

Sarna, M. J., & de Greve, J. P. 1996, QJRAS, 37, 11

Shara, M. M., Saffer, R. A., & Livio, M. 1997, ApJ, 489, L59

Sills, A., Karakas, A., & Lattanzio, J. 2008, arXiv:0811.2974

Sirianni, M., et al. 2005, PASP, 117, 1049

Sohn, Y.-J., Byun, Y.-I., & Chun, M.-S. 1996, Ap&SS, 243, 379

Stetson, P. B. 1987, PASP, 99, 191

Zinn, R., & Searle, L. 1976, ApJ, 209, 734

Table 1.   The BSS population of M2

Name	RA [degree]	DEC [degree]	m_{255}	U	B	V	I	r
BSS 1	323.3714411	-0.8178864	18.296	18.526	0.000	17.276	15.678	—
BSS 2	323.3696276	-0.8177717	17.413	17.460	0.000	17.828	16.353	—
BSS 3	323.3634359	-0.8316575	18.095	17.625	0.000	17.147	16.653	—
BSS 4	323.3622994	-0.8218842	18.652	18.077	0.000	17.638	16.720	—
....								

Note. — The complete table is available in electronic form.

Table 2.   Number Counts of BSS, HB, and RGB
Stars, and Fraction of Sampled Luminosity

r_i''	r_e''	N_{BSS}	N_{HB}	N_{RGB}	$L^{\mathrm{samp}}/L_{\mathrm{tot}}^{\mathrm{samp}}$
0	20	54	171	454	0.20
20	50	27	260	636	0.30
50	100	20	242	513	0.25
100	200	10	141	348 (2)	0.18
200	300	7	40	94 (3)	0.05
300	650	4 (1)	21	59 (12)	0.02

Note. — The values listed out of the parenthesis correspond to the number of stars assumed to belong to the cluster (and thus used in the analysis), while those in the parenthesis are estimated to be contaminating field stars (see Sect. 5.1).
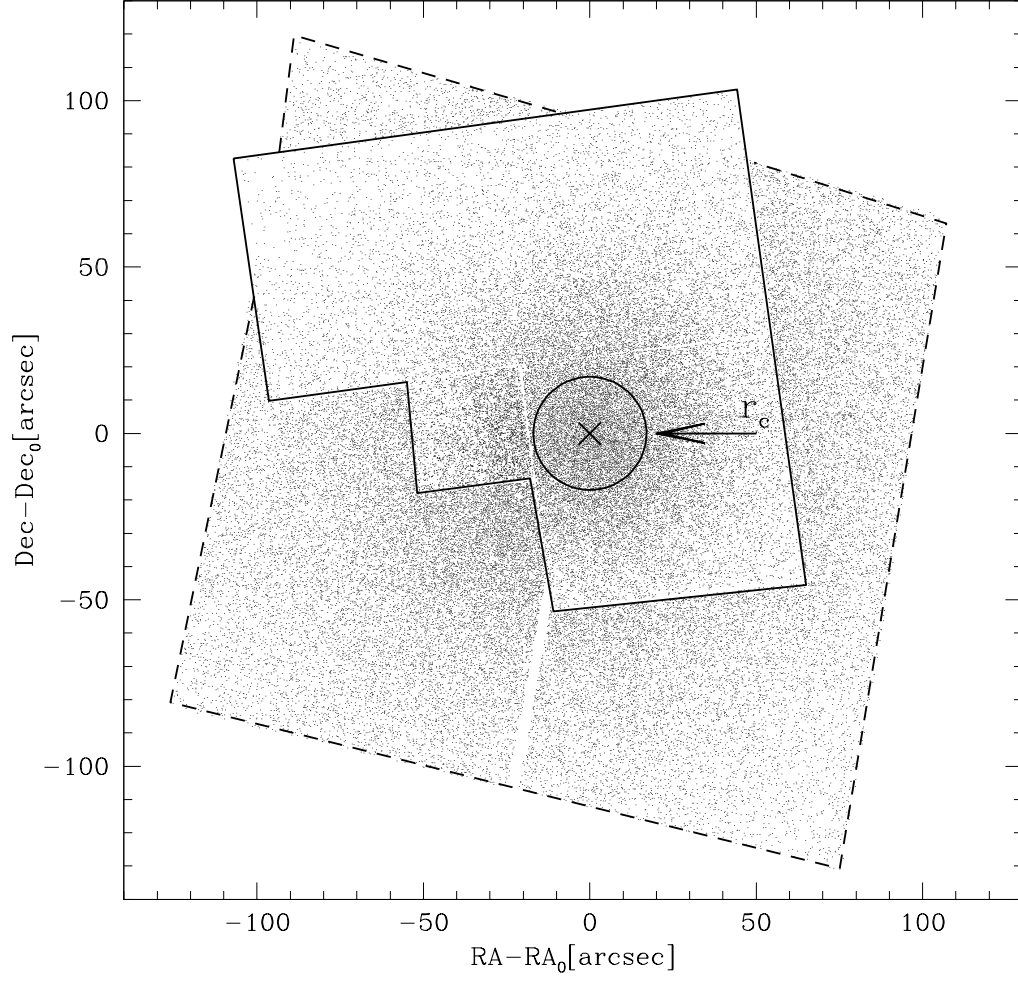
Fig. 1.— Map of the WFPC2 sample (solid line) and the ACS sample (dashed line) with the coordinates referred to the right ascension RA_0 and the declination Dec_0 of the cluster center of gravity (cross). The circle marks the core radius of the cluster as determined in Sect. 3.4.
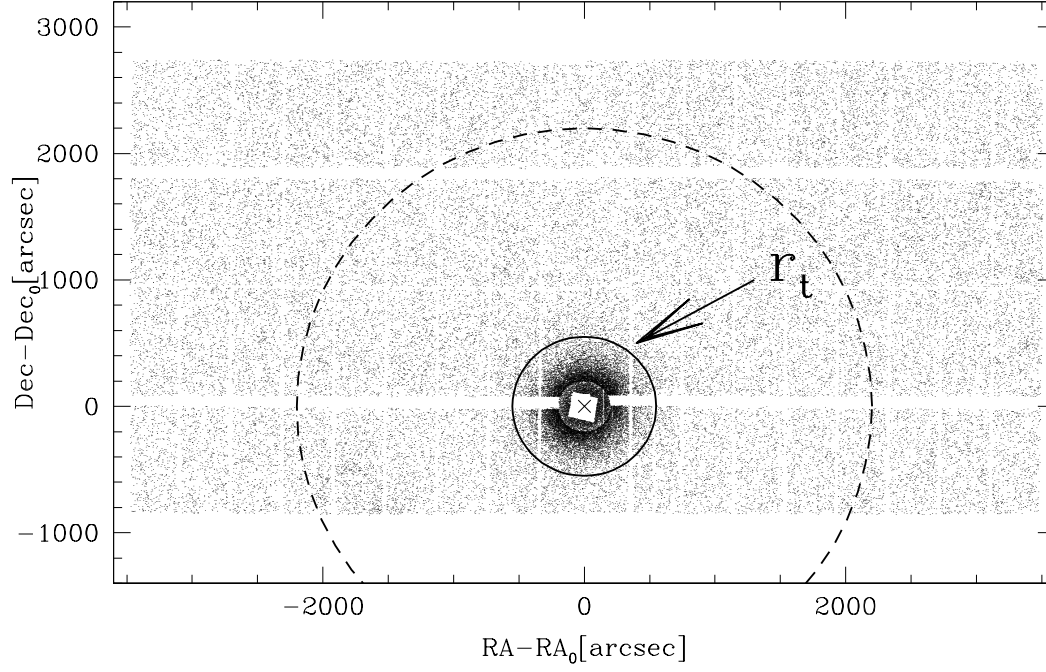
Fig. 2.— Map of the EMMI and MEGACAM/GALEX sample. The circle with radius $r_t = 550''$ marks the estimated tidal radius, while the dashed circle indicates the GALEX FOV.
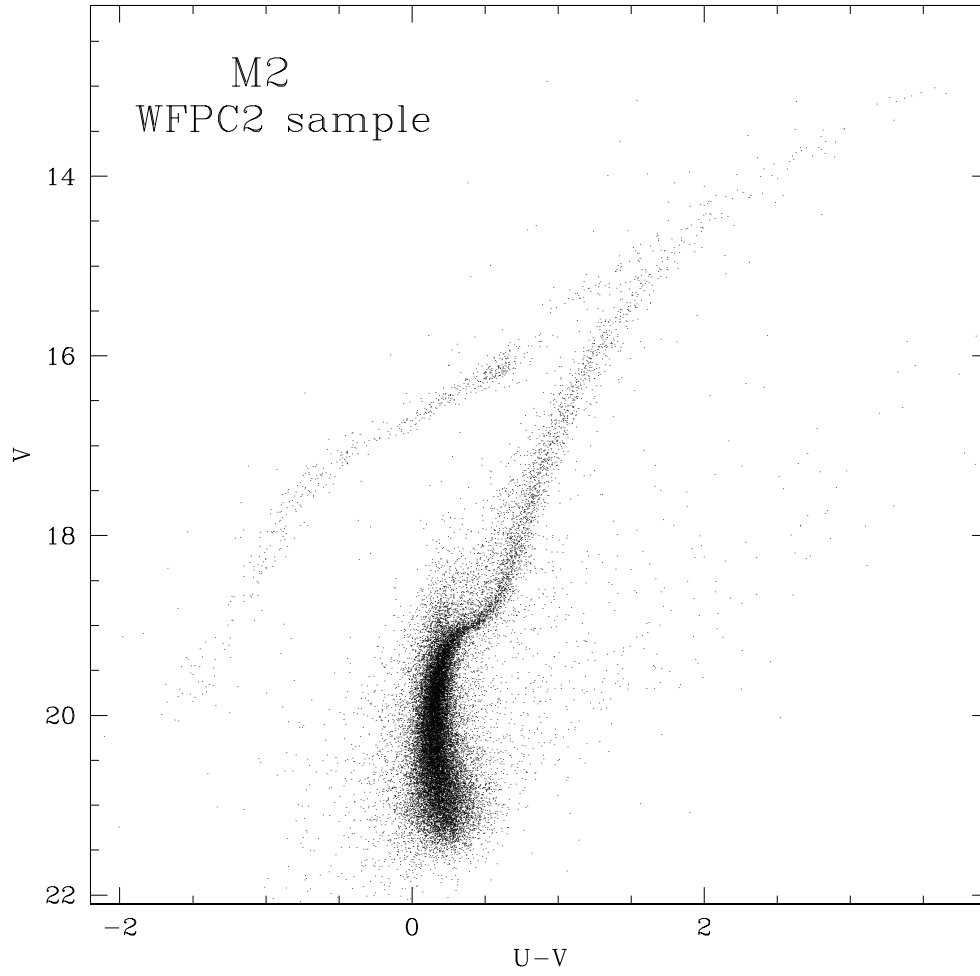
Fig. 3.— The $(V, U - V)$ CMD of the WFPC2 sample.
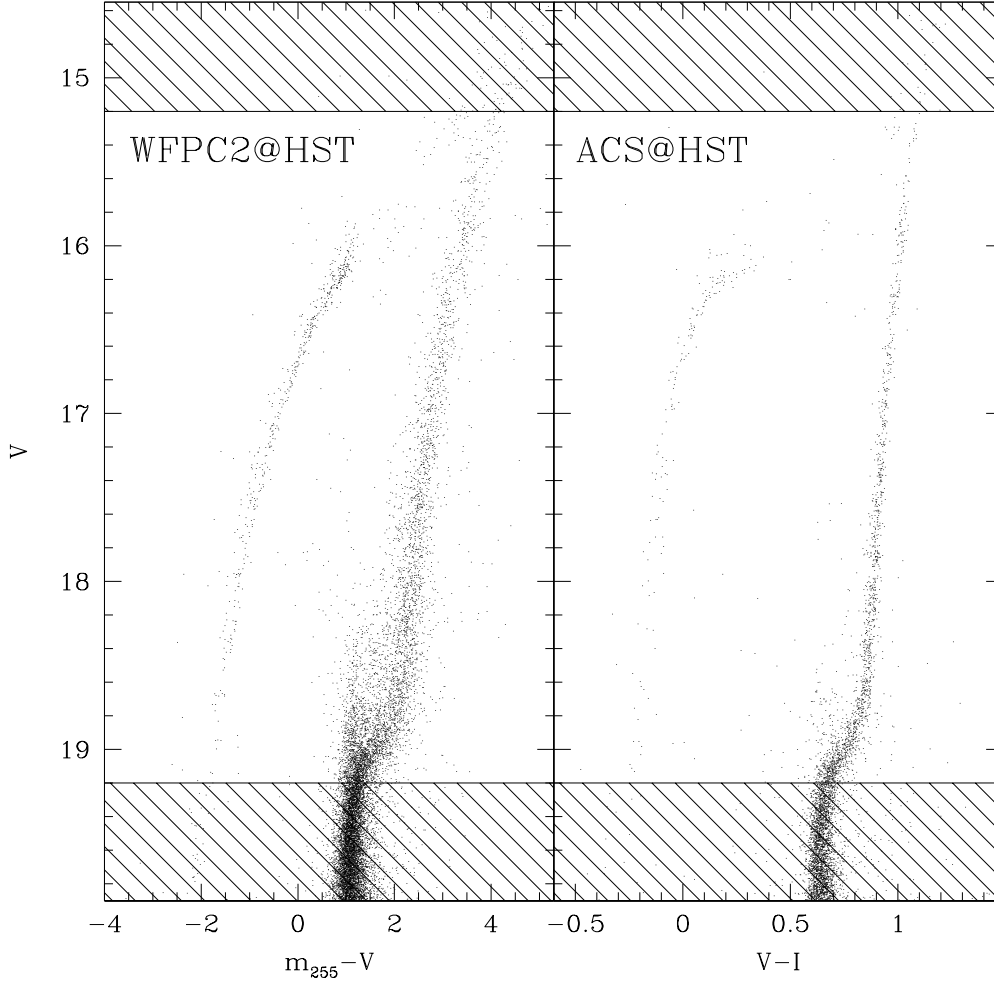
Fig. 4.— $(V, m_{255} - V)$ CMD of the stars lying in the WFPC2 FOV (left panel) and $(V, V - I)$ CMD of the stars detected in the ACS FOV complementary to WFPC2 (right panel). The shaded regions delimit the samples adopted to compute the star density profile (see Sect. 3.4).
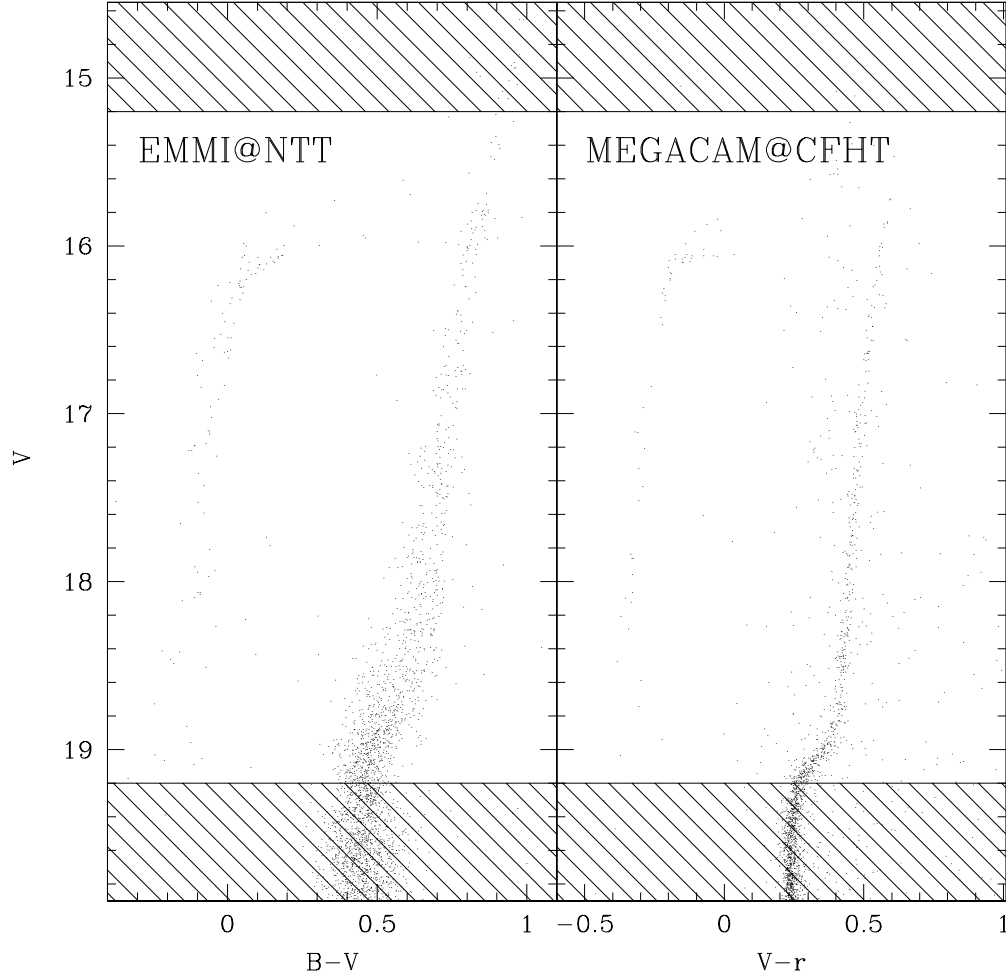
Fig. 5.— Optical CMDs of the EMMI (left panel) and the MEGACAM sample (right panel). The shaded region is as in Fig. 4
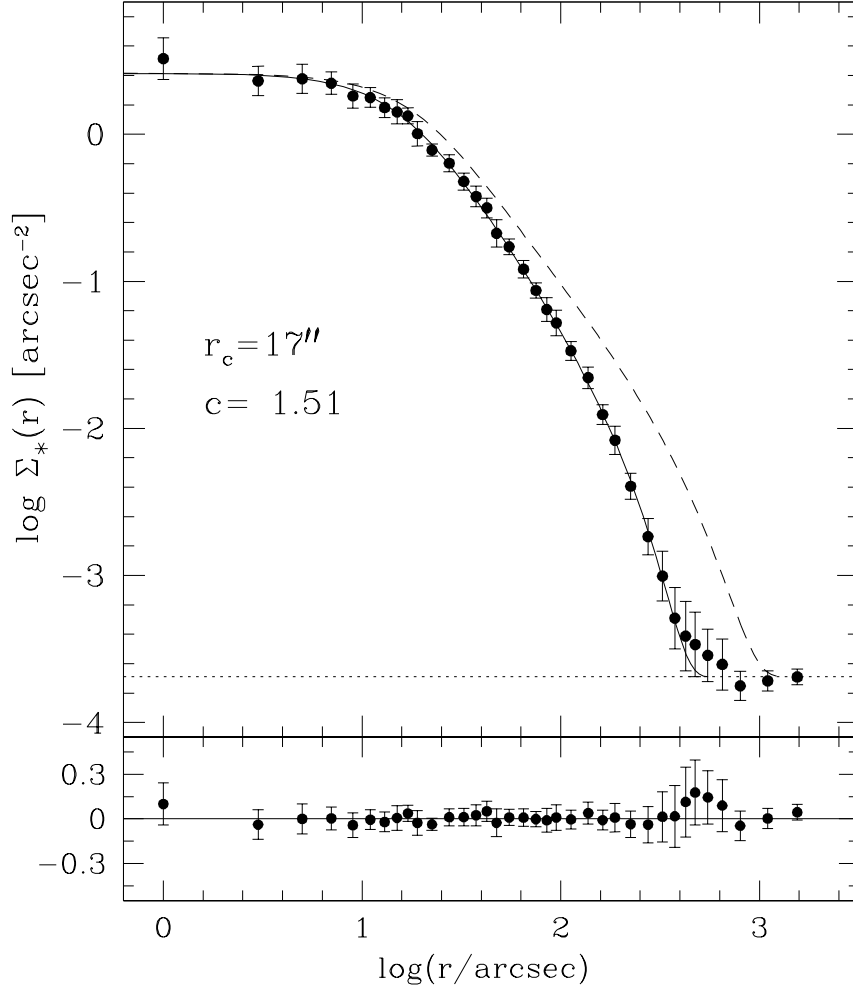
Fig. 6.— Observed surface density profile (dots and error bars) and best-fit King model (solid line). The radial profile is in units of number of stars per square arcsecond. The dotted line indicates the adopted level of the background (corresponding to 0.7 stars arcmin^{-2} in the range $15.2 < V < 19.2$). The model parameters are $r_c = 17''$ and $c = 1.51$. The lower panel shows the residuals between the observations and the fitted profile. The dashed line is the King-model obtained using the structural parameters quoted by Harris et al. (1996; see Sect. 3.4)
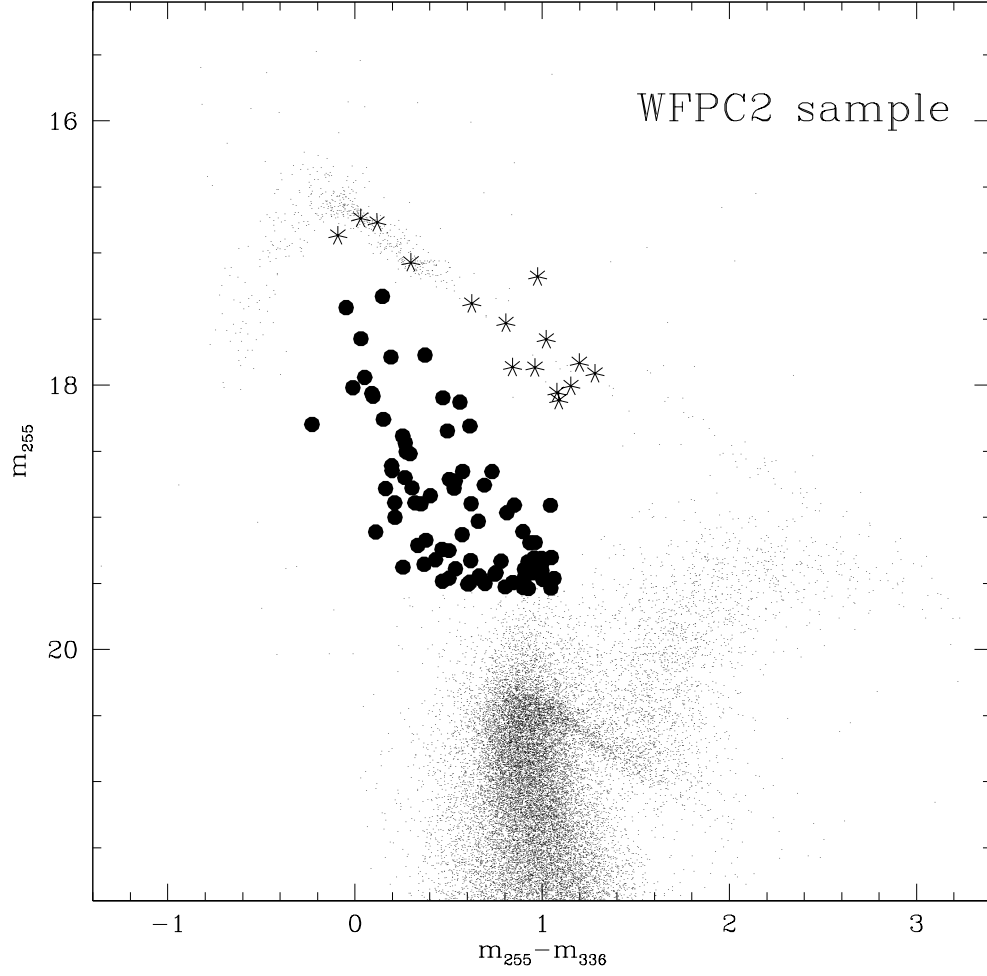
Fig. 7.— Ultraviolet CMD of the WFPC2 sample. The selected BSS population is marked as filled dots, and RR Lyrae stars as asterisks.
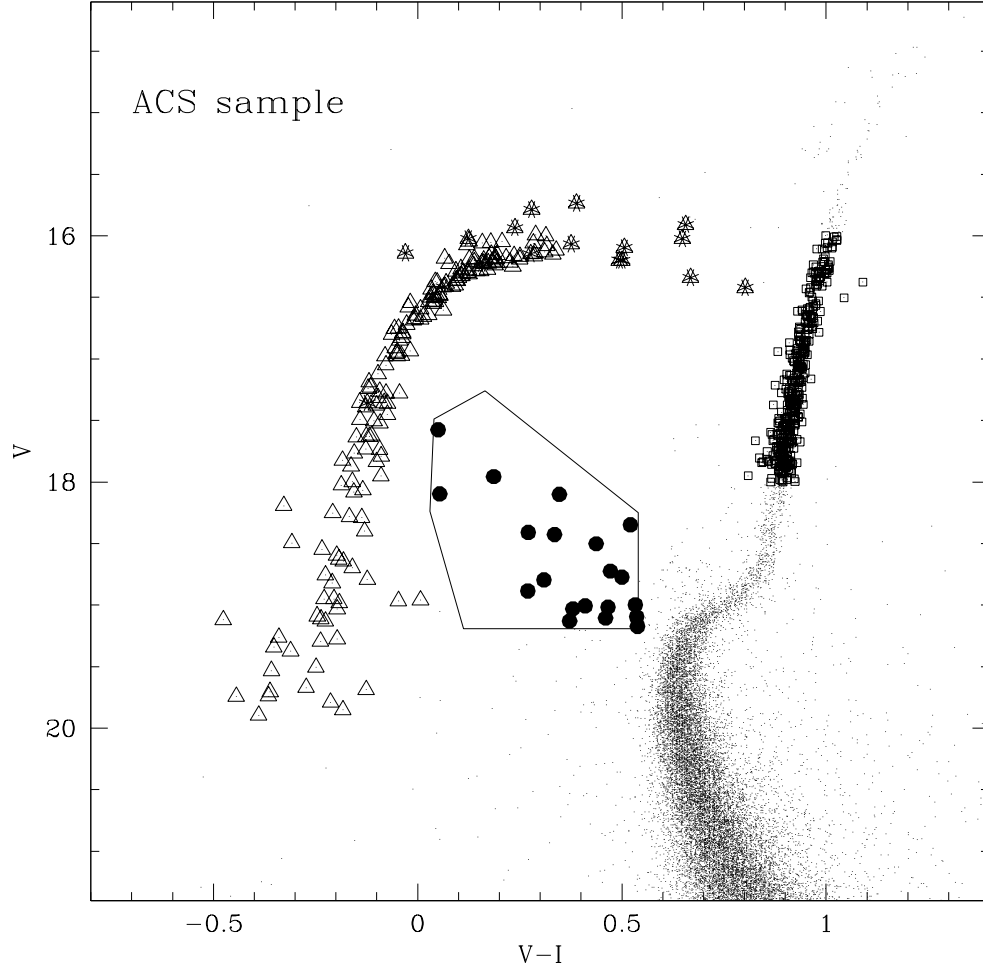
Fig. 8.— $(V, V - I)$ CMD of the ACS sample. The different stellar populations discussed in the paper are marked with different symbols (same as in Fig. 7 plus squares and triangles for the RGB and HB stars respectively).
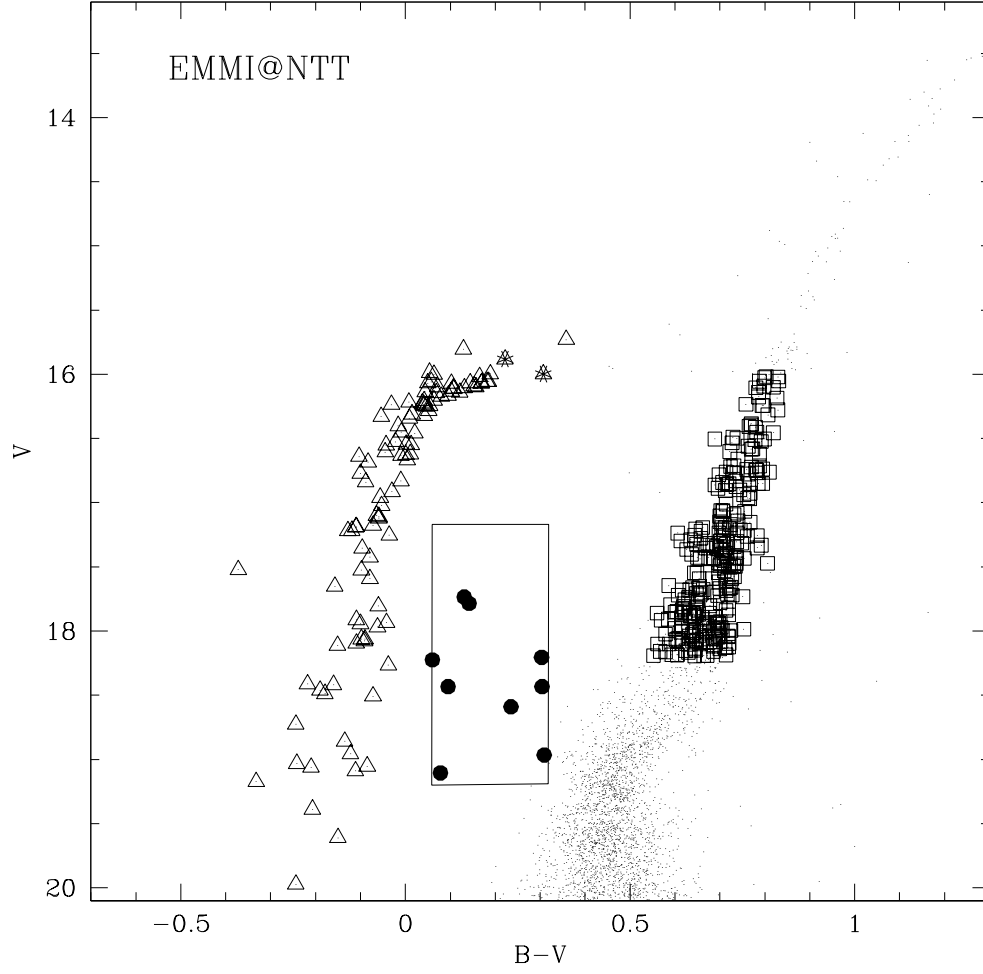
Fig. 9.— Optical CMD of the EMMI sample. The symbols have the same meaning as in Fig. 8.
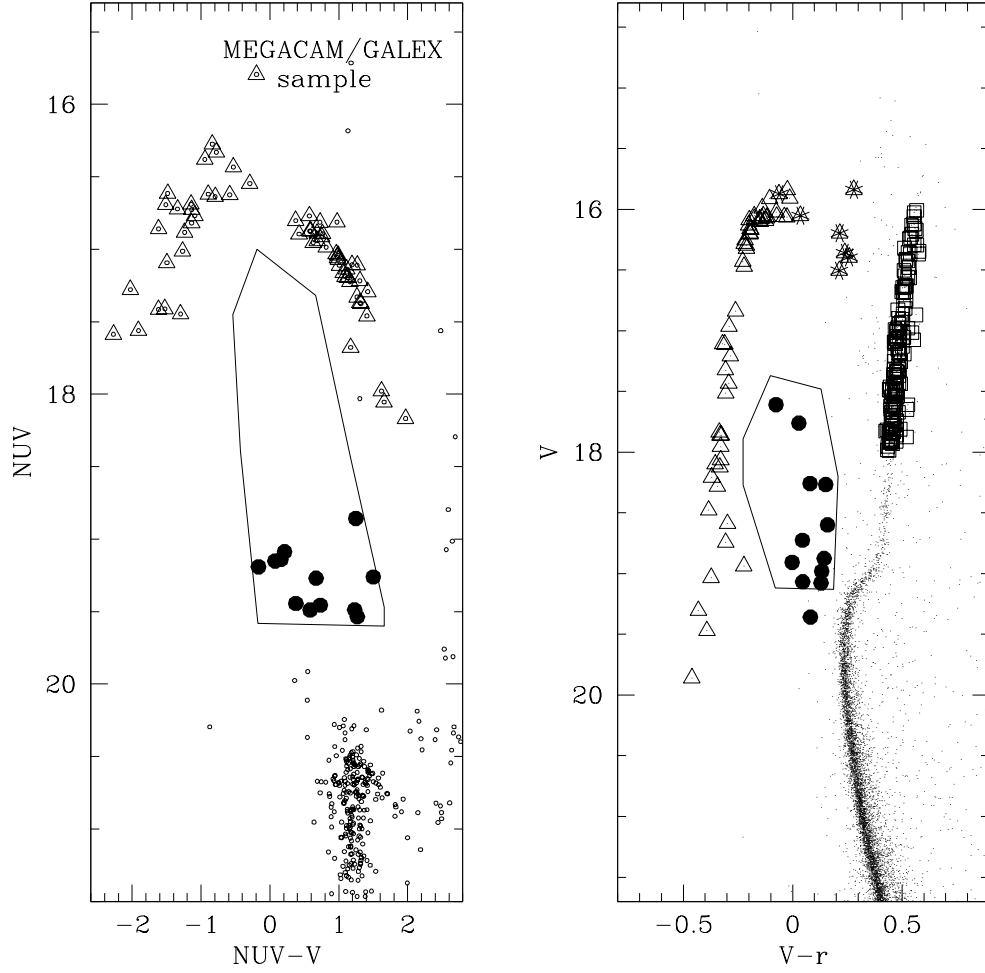
Fig. 10.— Ultraviolet (left panel) and optical (right panel) CMDs of the MEGA-CAM/GALEX sample. The NUV magnitudes have been obtained by matching the optical data with GALEX observations. The symbols have the same meaning as in Fig. 8.
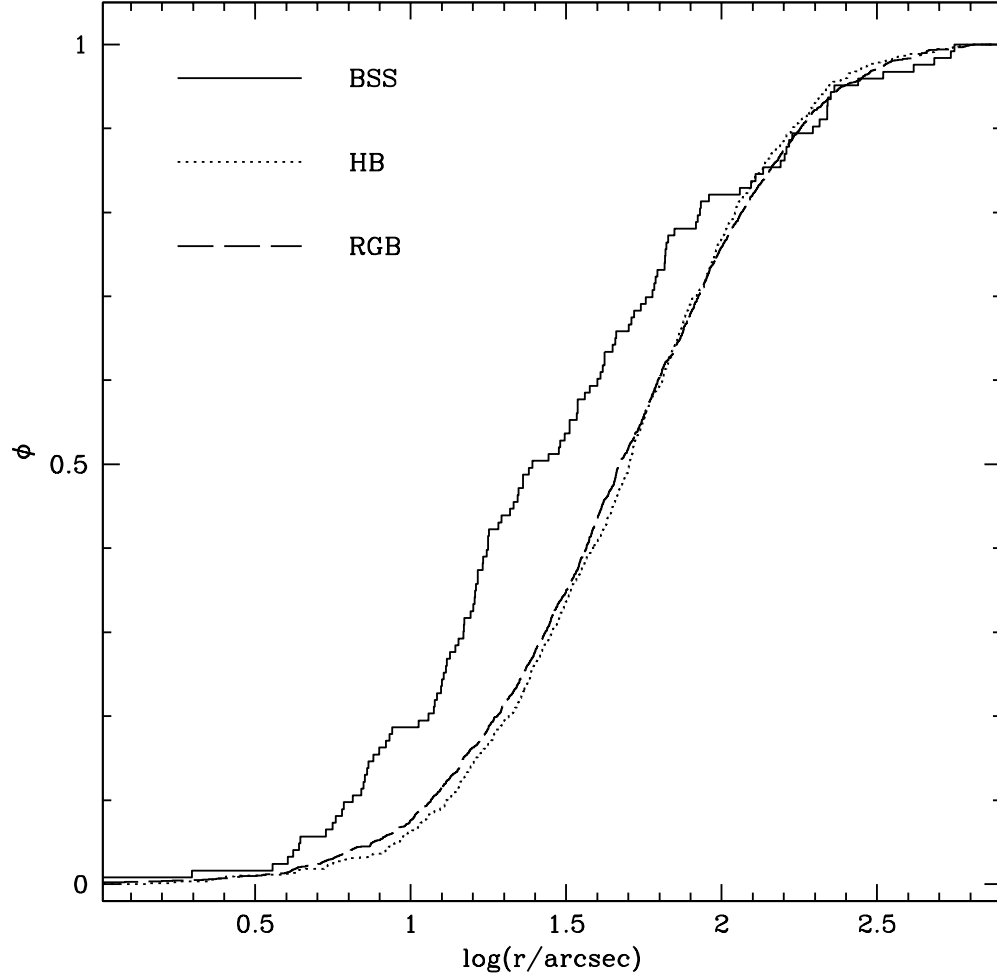
Fig. 11.— Cumulative radial distribution of BSS (solid line), HB (dotted line) and RGB (dashed line) stars as a function of the projected distance from C_{grav}.
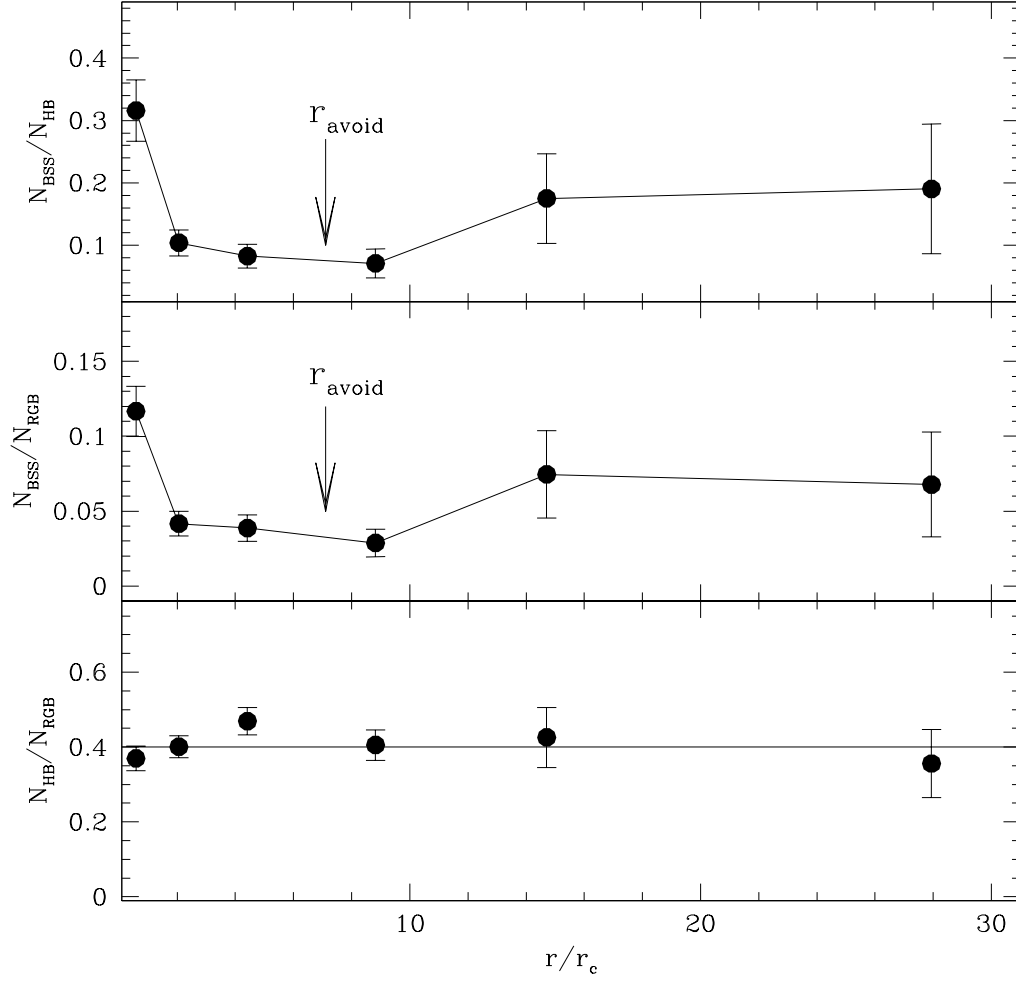
Fig. 12.— Radial distribution of the population ratios N_{HB}/N_{RGB}, N_{BSS}/N_{HB} and N_{BSS}/N_{RGB} as a function of the radial distance from the cluster center, expressed in units of the core radius. The arrows mark the position of the radius of avoidance (see Sect. 5).
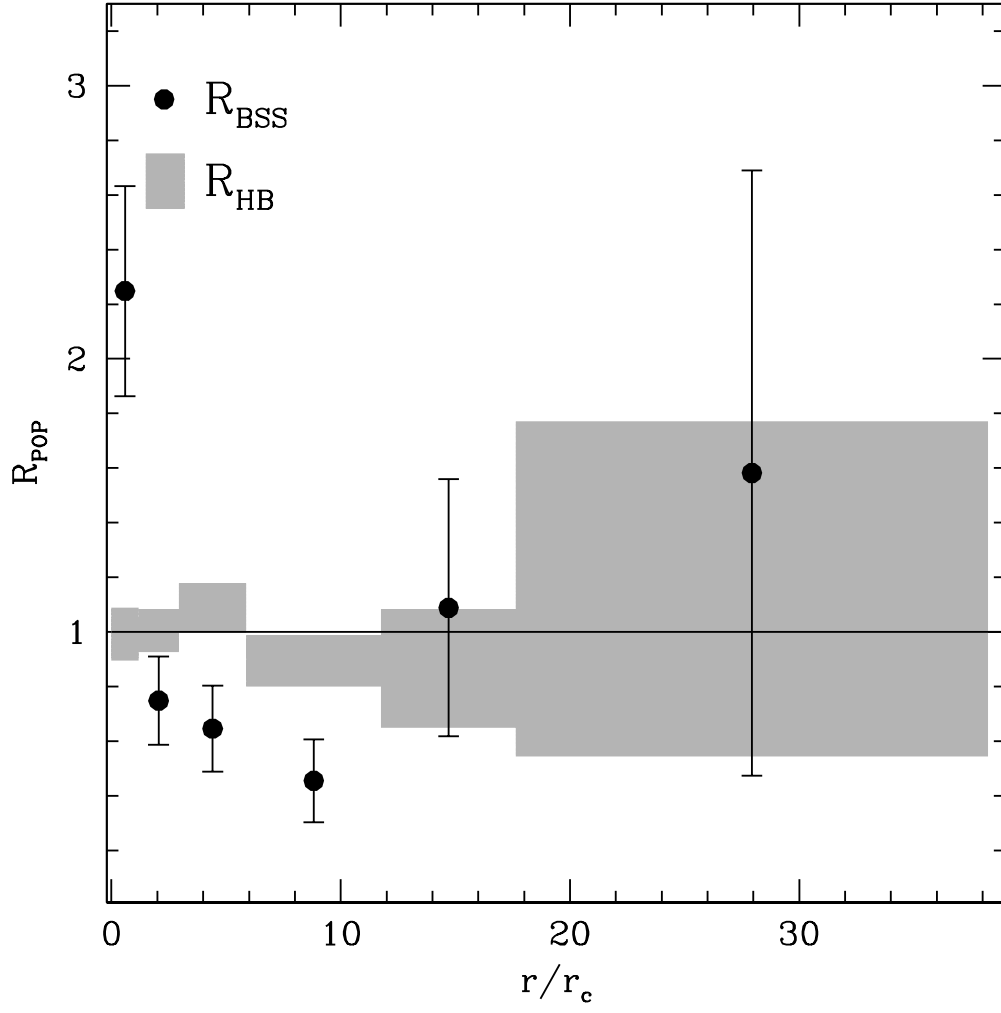
Fig. 13.— Radial distribution of the doubled normalized ratio of BSSs (large dots) and HB stars (grey rectangular regions). The vertical size of the grey rectangles correspond to the error bars.
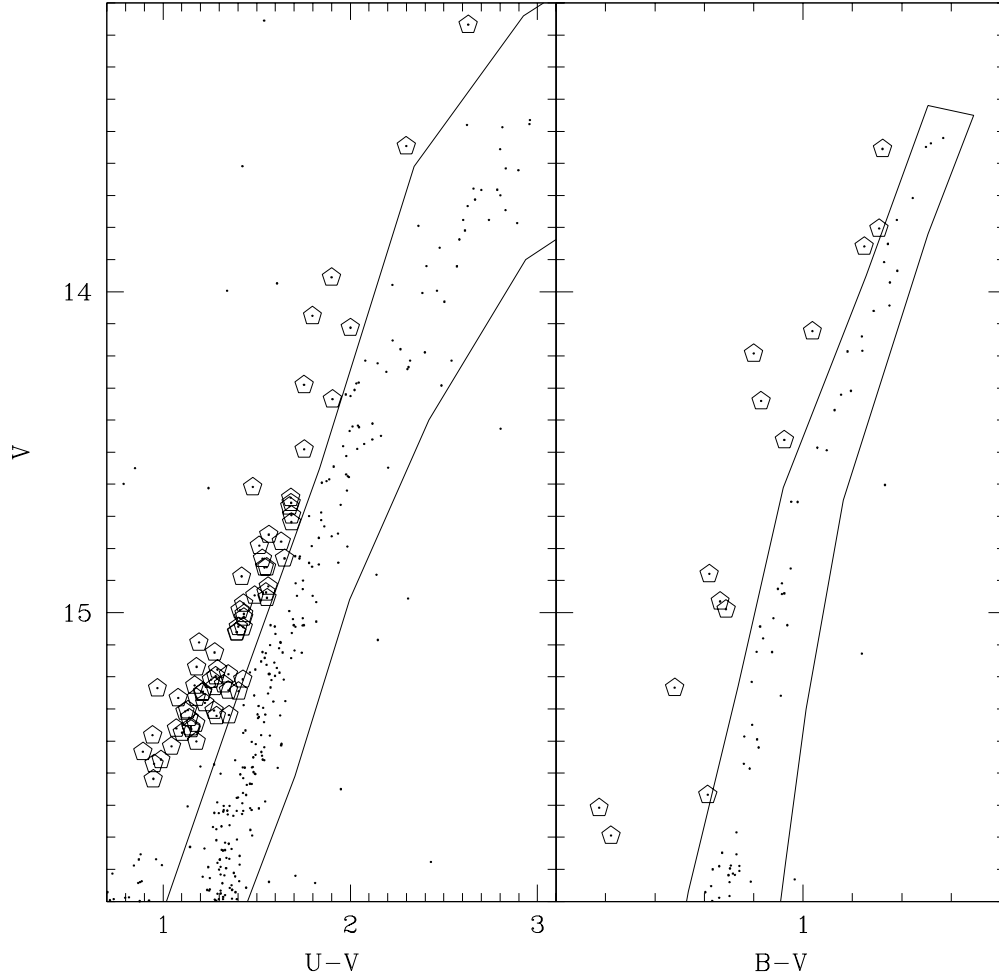
Fig. 14.— Brightest portion of the $(V, U - V)$ CMD for the WFPC2 sample (left panel) and of $(V, B - V)$ CMD for the EMMI sample (right panel). The selected AGB stars are marked as pentagons.
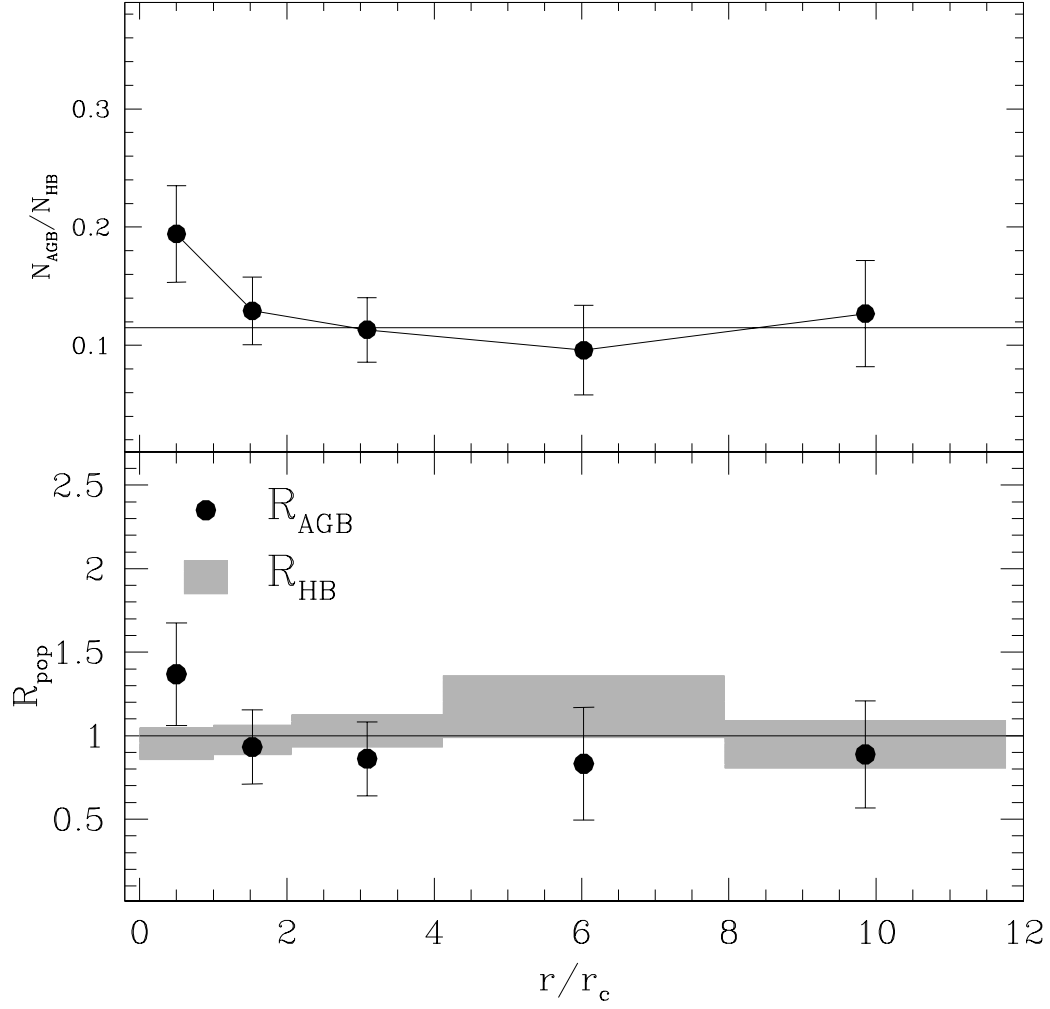
Fig. 15.— Radial distribution of the population ratios $N_{\mathrm{AGB}}/N_{\mathrm{HB}}$ (upper panel) and double normalized ratio (bottom panel) for AGB (dots) and HB (grey rectangles) as a function of the distance from C_{grav} in units of the core radius. The vertical size of the grey rectangles corresponds to the error bars.
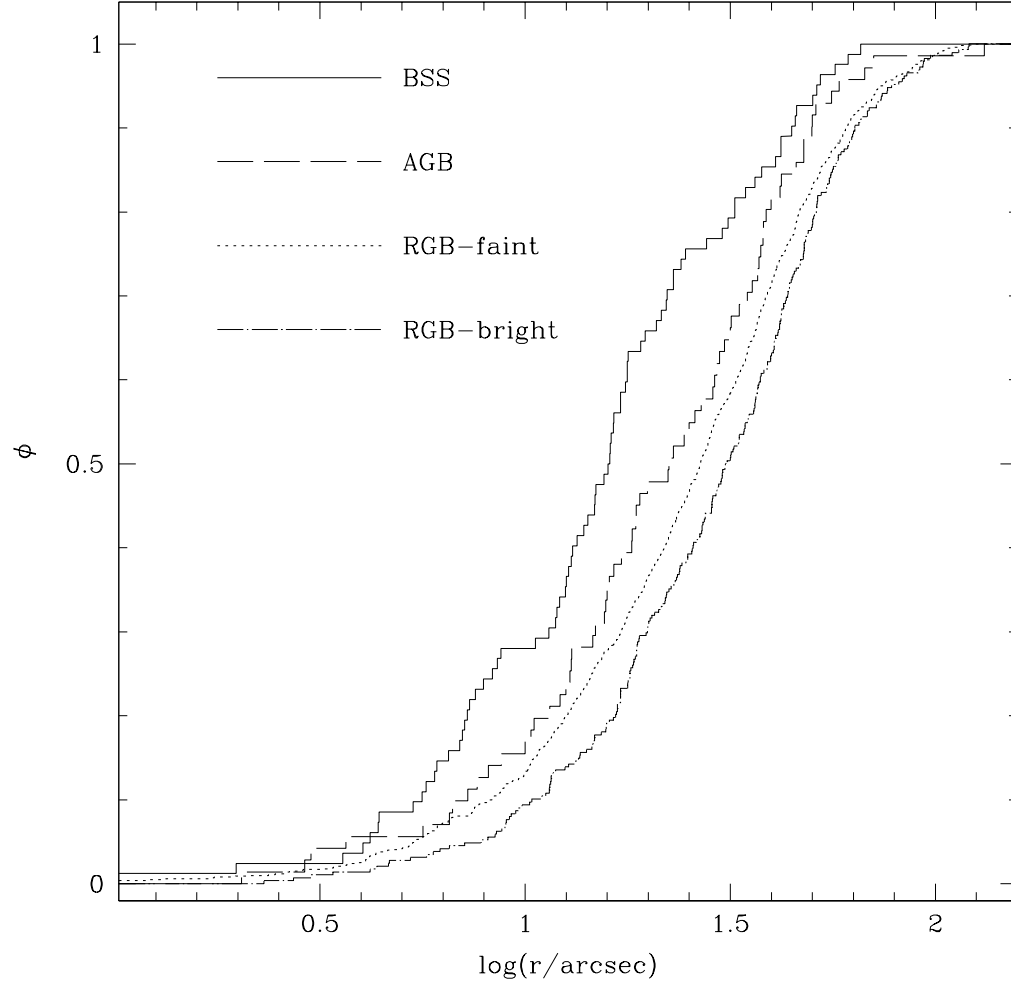
Fig. 16.— Cumulative radial distribution of BSS, AGB, bright-RGB and faint-RGB as selected in the WFPC2 sample.
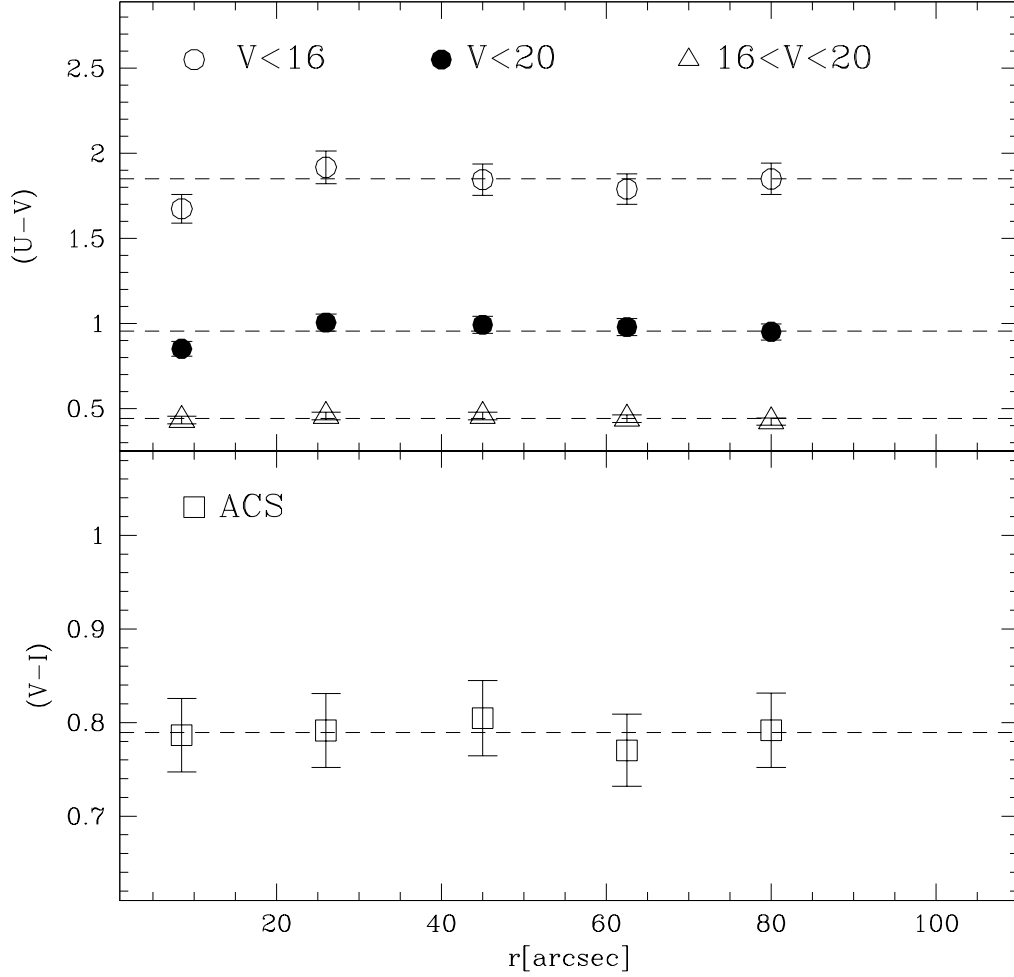
Fig. 17.— Top panel: radial distribution of the $(U - V)$ color computed from the WFPC2 resolved stars, for three different magnitude cuts (see labels). The dashed lines mark the average color computed from the four most external points. Lower panel: same for the $(V - I)$ color computed from the ACS sample.
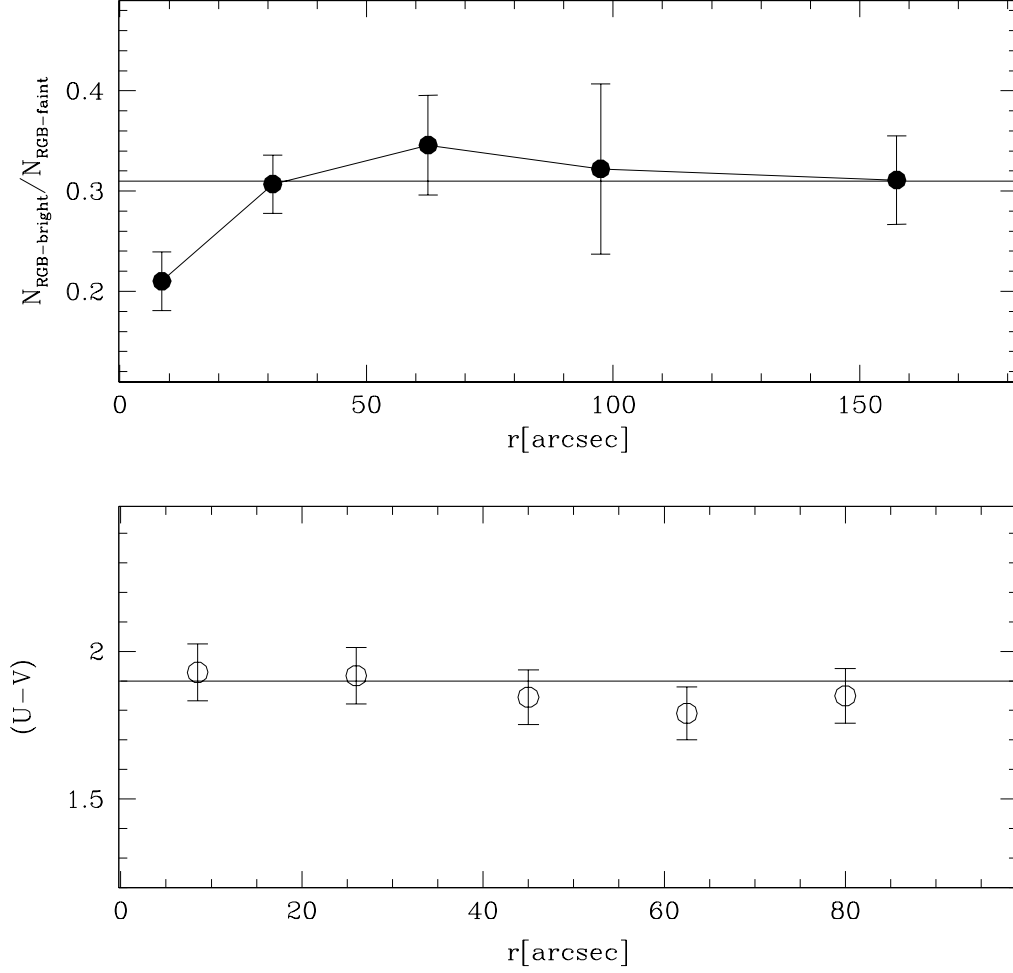
Fig. 18.— Upper panel: radial distribution of the ratio between the number of bright $(V < 16)$ and faint $(V \geq 16)$ RGB stars in the WFPC2 and EMMI samples. In order to increase the central value of this ratio to the average one, ~ 25 stars should be added to the bright RGB population within the cluster core. Lower panel: the $(U - V)$ color obtained by adopting such an increase is shown panel.